PAPER

Check for updates

Efficient ammonia photosynthesis from nitrate by graphene/Si Schottky junction integrated with Ni–Fe LDH catalyst†

Chun-Hao Chiang, [ID] ‡[a] Yu-Ting Kao,‡[a] Po-Hsien Wu,[a] Ting-Ran Liu,[a] Jia-Wei Lin,[b] Po-Tuan Chen,[c] Jr-Wen Lin,[a] Shan-Chiao Yang, [ID] [a] Hsuen-Li Chen, [ID] [a] Shivaraj B. Patil,[d] Di-Yan Wang [ID] *[d] and Chun-Wei Chen [ID] *[abe]

This work presents stable and efficient photoelectrochemical (PEC) nitrate-to-ammonia conversion through the facile integration of a graphene/Si Schottky junction and earth-abundant Ni–Fe layered double hydroxide (LDH). Efficient charge separation for photogenerated carriers and large photovoltage generation can be achieved resulting from the graphene/Si Schottky junction photocathode. Through the atomic layer of graphene, the direct growth of the Ni–Fe LDH catalyst on the graphene/Si Schottky junction by electrodeposition provides excellent quality at the interfaces between the catalyst and photocathode. The Ni–Fe LDH/graphene/Si Schottky junction photocathode exhibits a promising and stable PEC conversion from nitrate to ammonia, with an optimal onset potential of 0.17 V *vs.* the reversible hydrogen electrode (RHE), the largest saturated photocurrent density of -31.9 mA cm^{-2}, and the highest faradaic efficiency of 92.5% at 0.15 V *vs.* RHE. Combined with the several advantages of graphene, such as inherent chemical inertness, high optical transparency, and excellent conductivity, the integration of the semiconductor LDH catalyst on the graphene/Si Schottky junction platform provides an effective strategy to achieve stable and efficient PEC nitrate-to-ammonia conversion.

Introduction

Ammonia (NH$_3$) has always been ranked in the list of high-demand goods owing to its wide application, including fertilizers, dyes, synthetic fibers, chemicals, pharmaceuticals, *etc.* The industrial Haber–Bosch process is widely used to produce ammonia on a large scale and is an energy-intensive process with harsh reaction conditions such as high temperature and pressure, leading to high operational costs. Recently, a more sustainable approach by the aqueous-based electrocatalytic (EC) nitrogen reduction reaction (NRR) controlled by applying electrical potentials under ambient conditions has attracted significant research interest.[1] Many efforts to explore various

catalysts for the EC NRR have been reported in the past decade.[2,3] However, due to the poor nitrogen (N$_2$) solubility in water and high dissociation energy of the N≡N bond (941 kJ mol^{-1}) under ambient conditions, the electrocatalytic conversion rate of nitrogen to ammonia is limited, and this inevitably causes an inferior performance.[4] There has been a recent upsurge in scientific research for alternative nitrogen sources for the EC reaction of ammonia synthesis. The nitrate anion (NO$_3^-$), which has a relatively low dissociation energy of the N=O bond (204 kJ mol^{-1}) compared with that of the N≡N bond[5] and has a superior solubility in water compared to nitrogen gas,[6] exhibits much better reaction kinetics for ammonia production. Another advantage of using nitrate as the source of EC ammonia synthesis is its rich abundance in nature, particularly in current environmental pollutants originating from the excessive use of fertilizers for the production of crops or livestock.[7] Therefore, the mass production of ammonia from nitrate has the potential not only to produce renewable energy but also help to reduce environmental pollution. The development of various catalysts for the efficient synthesis of ammonia by the EC nitrate reduction reaction (NTRR) has been demonstrated, such as copper-incorporated crystalline 3,4,9,10-perylenetetracarboxylic dianhydride (PTCDA),[8] TiO$_2$,[9] Cu/Ni alloy,[10] CuO nanowire arrays,[11] and Co–Fe layered double hydroxide (LDH).[12] These catalysts exhibit promising performances for the EC NTRR with the highest faradaic efficiency of

[a]*Department of Materials Science and Engineering, National Taiwan University, Taipei 10617, Taiwan. E-mail: chunwei@ntu.edu.tw*

[b]*Center for Condensed Matter Sciences, National Taiwan University, Taipei 10617, Taiwan*

[c]*Department of Vehicle Engineering, National Taipei University of Technology, Taipei 10608, Taiwan*

[d]*Department of Chemistry, Tunghai University, Taichung 40704, Taiwan. E-mail: diyanwang@thu.edu.tw*

[e]*Center of Atomic Initiative for New Materials (AI-MAT), National Taiwan University, Taipei 10617, Taiwan*

† Electronic supplementary information (ESI) available. See DOI: https://doi.org/10.1039/d3ta01169k

‡ These authors contributed equally to this work.

This journal is © The Royal Society of Chemistry 2023

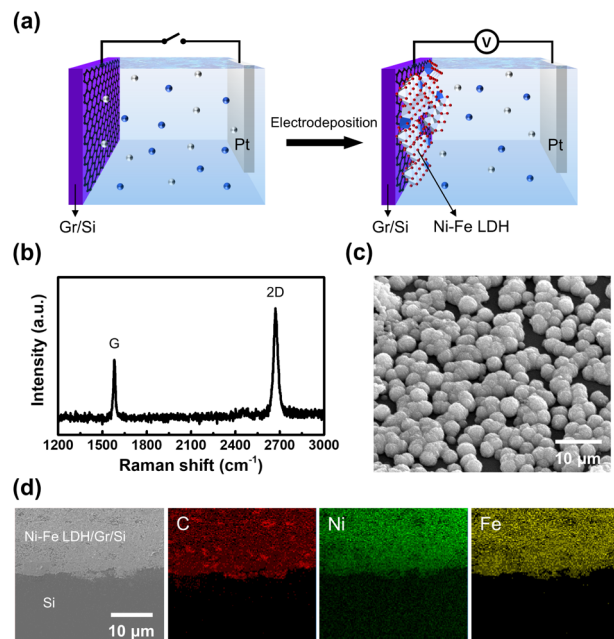*J. Mater. Chem. A*, 2023, 11, 11179–11186 | 11179

over 80%. Compared to the EC approach, the photo-electrochemical (PEC) system, which directly utilizes solar energy either to perform water splitting or to convert carbon dioxide (CO_2) or nitrogen into value-added chemicals, provides a promising platform for solar-to-fuel conversion.[2,13,14] In particular, the conversion of nitrate to ammonia using renewable solar energy may provide a sustainable alternative for ammonia production from both the energy and environment aspects. Although the promising progress of the EC NTRR based on the abovementioned catalysts has been demonstrated, there are only a few reports on the synthesis of ammonia from nitrate based on the PEC approach, such as using Au-decorated ordered silicon nanowires[15] and TiO_x/CdS/Cu_2ZnSnS_4 (CZTS) photocathodes.[16] However, their current densities and NH_3 yield rates haven't caught up with the reported values by EC methods. There is still a lot of room for further development.

Silicon (Si) is a widely used material in the electronics and photovoltaic industries. It comprises a relatively low band gap that enables significant absorption under solar irradiation and has mature fabrication technology. The integration of various catalysts with Si has attracted great attention to develop feasible PEC photoelectrodes for efficient solar-to-fuel conversions such as water splitting and carbon and nitrogen fixation.[17–19] However, a critical challenge for Si photoelectrodes is their poor stability in an aqueous solution.[20] Ultrathin oxide layers by atomic layer deposition (ALD) are usually used as a protective layer to enhance PEC cell stability because they have inert chemical activities.[21,22] Therefore, the integration of a thin protective layer and an effective non-opaque catalyst with a Si absorber becomes the crucial issue for a high-performance PEC device for solar-to-fuel conversion. Transition-metal-based LDHs, owing to their abundance in the earth's crust and unique catalytic properties, have become an important class of materials as efficient electrocatalysts for the hydrogen evolution reaction (HER), oxygen evolution reaction (OER), carbon dioxide reduction reaction (CO_2RR), NRR and NTRR.[12,23] For example, Ni–Fe LDH has demonstrated excellent performance with unique bifunctional catalytic properties for both the HER and the OER, and great stability in a basic environment.[24] An N-doped LDH-derived NiZnAl oxide was synthesized on a reduced graphene oxide substrate for the electrocatalytic CO_2RR to produce carbon monoxide (CO).[25] In addition, Co–Fe LDH was recently demonstrated as a highly efficient NTRR electrocatalyst for ambient ammonia synthesis with excellent activity, selectivity, and stability.[12] Although transition-metal-based LDHs demonstrate excellent electrocatalytic performances for various EC conversion reactions, the integration of a LDH with Si photoelectrodes for PEC solar-to-fuel conversion is still a challenging task because of poor adhesion between the Si and LDH catalyst. Typically, a thin and conductive interlayer such as nickel or titanium is deposited on Si photoelectrodes to grow LDH catalysts by hydrothermal or electrodeposition methods.[26,27] However, the light-blocking issue for those devices using a thin metallic adhesive layer between Si and the LDH catalyst is inevitable and may sacrifice the light-harvesting efficiency for PEC conversion.

Graphene (Gr), which has a single-atom-thick plane of carbon atoms arranged in a honeycomb lattice, exhibits excellent carrier transport and high transparency due to its unique two-dimensional (2D) energy dispersion band structure.[28] Graphene/Si Schottky junction solar cells exhibiting promising photovoltaic conversion efficiencies have been demonstrated recently, where the formation of a Schottky junction with a single atomic layer of graphene and Si enables efficient charge separation for photogenerated carriers.[29] In this work, we demonstrate stable and efficient PEC nitrate-to-ammonia conversion through the facile integration of Si and an earth-abundant Ni–Fe LDH catalyst with an atomic layer of graphene. The direct growth of Ni–Fe LDH on the graphene/Si Schottky junction photocathode exhibits several unique advantages due to the multi-functional interlayer of graphene. For example, because a single layer of graphene shows high transparency with 97.7% transmittance,[30] the light-blocking issue for the integrated Ni–Fe LDH/graphene/Si PEC devices can be avoided, and the corresponding light-harvesting efficiency of these devices can be enhanced. The formation of a graphene/Si Schottky junction enables efficient charge separation for photogenerated carriers, resulting in enhanced PEC performance. In addition, the inherent chemical inertness of graphene also significantly improves the operational stability of graphene/Si junction photocathodes. The direct growth of Ni–Fe LDH on the surface of the graphene/Si Schottky junction exhibits excellent quality at the interfaces between the catalyst and photocathode, leading to an outstanding PEC NTRR performance. The PEC device consisting of the Ni–Fe LDH/graphene/Si heterojunction photocathode exhibits a positive shift of 550 mV compared to the dark control, resulting from the photovoltage generation at the graphene/Si Schottky junction. A promising PEC NTRR performance with a faradaic efficiency of 85% at a potential of −0.25 V *vs.* the reversible hydrogen electrode (RHE) can be achieved at the Ni–Fe LDH/graphene/planar Si Schottky junction photocathode. Furthermore, the PEC NTRR performance can be improved by utilizing 3D pyramid Si to replace the planar Si to enhance the light-harvesting efficiency. The Ni–Fe LDH/graphene/pyramid Si Schottky junction photocathode exhibits the highest faradaic efficiency of 92.5% at a potential of 0.15 V *vs.* RHE. Combined with the inherent chemical inertness of graphene, our results suggest that the facile integration of the semiconductor LDH catalyst on a graphene/Si Schottky junction platform provides an effective strategy to achieve stable and efficient PEC nitrate-to-ammonia conversion.

Results and discussion

The direct growth of the Ni–Fe LDH catalyst on the surface of the graphene/Si Schottky junction by electrodeposition is illustrated schematically in Fig. 1a. The graphene/Si Schottky junction was prepared by transferring chemical vapor deposition (CVD)-grown single-layer graphene onto a p-type lightly doped Si substrate (p-Si) by the polymer-assisted transfer method.[17,31] The details of the graphene transfer are described in the Experimental section. Fig. 1b presents the typical Raman

11180 | *J. Mater. Chem. A*, 2023, **11**, 11179–11186

This journal is © The Royal Society of Chemistry 2023

Fig. 1   Direct electrodeposition of the Ni–Fe LDH on the graphene/Si Schottky heterojunction. (a) The schematic illustration of electrodeposition of Ni–Fe LDH on the graphene/Si Schottky junction. (b) Raman spectrum of single-layer graphene, which is transferred on Si. (c) The morphology of electrodeposited Ni–Fe LDH nanoparticles. (d) Auger elemental/chemical mapping analysis of the selective Ni–Fe LDH growth on the graphene/Si junction.

characteristic G and 2D peaks centered at 1579.8 cm^{-1} and 2670.4 cm^{-1} of single-layer graphene on Si.[32] The absence of a defect-related D peak around 1350 cm^{-1} implies the high quality of the CVD-grown graphene. The graphene/Si Schottky junction was then placed into the electrodeposition cell and wired to a potentiostat for electrodeposition. A platinum wire and Ag/AgCl (3 M KCl) were used as the counter and reference electrodes, respectively. The electrodeposition aqueous solution consists of nickel sulfate and iron sulfate as the main Ni–Fe LDH precursors, boric acid for pH value control, and sodium chloride for helping adhesion.[33] Because of the excellent conductivity of graphene, the direct growth of Ni–Fe LDH on the surface of graphene/Si by electrodeposition can be achieved. Fig. 1c shows the corresponding scanning electron microscopy (SEM) image of the as-deposited Ni–Fe LDH nanoparticles (NPs) with a diameter from 200 nm to 400 nm grown on the surface of the graphene/Si Schottky junction. Fig. 1d shows the Auger elemental/chemical mapping of the selective Ni–Fe LDH electrodeposition on the graphene/Si Schottky junction, where two separate regions with and without graphene covering on the Si substrate were intentionally created. In the leftmost part of Fig. 1d, a secondary electron image clearly reveals an apparent boundary line between the two areas after electrodeposition. The electrodeposition of Ni–Fe LDH NPs only occurs at the graphene/Si Schottky junction, while there are negligible Ni–Fe LDH NPs in the other area of the pristine Si without graphene. The corresponding Auger elemental/chemical mapping images of C, Fe, and Ni elements in Fig. 1d (from left to right) provide us

with information to confirm the uniform composition distribution by the direct growth of Ni–Fe LDH on the graphene/Si Schottky junction. These images indicate that the pristine Si is not an appropriate platform for the electrodeposition of Ni–Fe LDH. By contrast, the selective growth of Ni–Fe LDH on the surface of the graphene/Si junction is attributed to a low-resistance pathway for electrodeposition on single-layer graphene. The charge transfer resistances (R_{ct}) of the pristine Si and graphene/Si junction are further measured via electrochemical impedance spectroscopy (EIS) in the electrodeposition solution, as mentioned above. The corresponding Nyquist plots in Fig. S2† showed that the R_{ct} extracted from the fitted equivalent circuit of graphene/Si is about four orders of magnitude lower than that of pristine Si. The result indicated a more efficient charge carrier transfer and facile electrodeposition reaction on the surface of the graphene/Si Schottky junction compared to pristine Si.

To further examine the interface quality at the Ni–Fe LDH/graphene/Si junction, cross-sectional transmission electron microscopy (TEM) analysis was performed as shown in Fig. 2a and b. Carbon and platinum protection layers were deposited on the surface to prevent the sample from being damaged during the focused-ion beam (FIB) process. Fig. 2b shows the
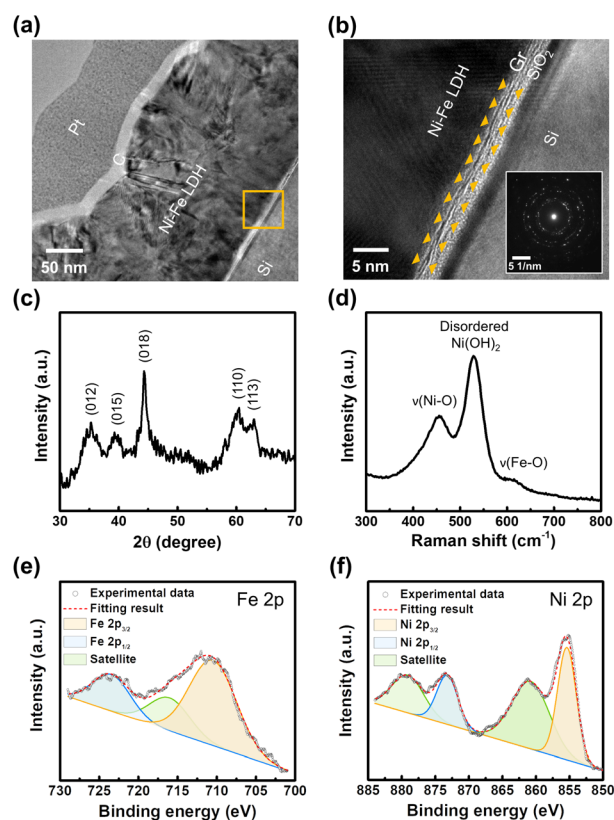
Fig. 2   Material characterization of the as-deposited Ni–Fe LDH. (a) The cross-sectional TEM image of the Ni–Fe LDH/graphene/Si Schottky junction. (b) The zoomed-in image of the highlighted rectangular area in (a). (c) XRD spectrum of as-deposited Ni–Fe LDH. (d) Raman spectrum of as-deposited Ni–Fe LDH on the graphene/Si junction. The high-resolution XPS spectra of (e) Fe 2p and (f) Ni 2p of the Ni–Fe LDH.

This journal is © The Royal Society of Chemistry 2023

J. Mater. Chem. A, 2023, 11, 11179–11186 | 11181

zoomed-in image of the highlighted rectangular area in Fig. 2a. It is seen that the direct growth of the Ni–Fe LDH catalyst on the surface of the graphene/Si junction exhibits excellent interface quality without the appearance of pores or holes at the interface. The formation of a high-quality interface between the Ni–Fe LDH catalyst and graphene/Si junction is particularly important for a high-performance PEC electrode and allows the photogenerated electrons at the Si absorber to be efficiently transported toward the catalyst and electrolyte for the EC reaction. The inset of Fig. 2b shows the selected area electron diffraction (SAED) pattern of the Ni–Fe LDH, where the multiple diffraction rings indicate the polycrystalline feature of the electrodeposited Ni–Fe LDH.[34] In addition to the SAED pattern on the local area, the crystallinity of the millimeter-scale Ni–Fe LDH thin film on the graphene/Si Schottky junction was also characterized by X-ray diffraction (XRD) analysis (Fig. 2c). A series of Bragg reflections match well with the LDH structure. The XRD spectrum presents several diffraction peaks of (012), (015), (018), (110), and (113) crystal planes at 35.0°, 39.6°, 44.3°, 60.0°, and 63.0°, respectively, which are consistent with the typical crystal structure of Ni–Fe LDH.[35] According to the above results from the SAED and XRD patterns, the Ni–Fe LDH grown on the graphene/Si Schottky junction by electrodeposition exhibits coexisting amorphous and polycrystalline structures.

The direct growth of Ni–Fe LDH on the surface of the graphene/Si Schottky junction can be further supported by Raman spectroscopy and X-ray photoelectron spectroscopy (XPS) analyses. Fig. 2d exhibits the distinct Raman peaks at 455.4 cm^{-1}, 528.4 cm^{-1}, and 614.7 cm^{-1}, which are attributed to the Ni–O band,[36] defective or disordered $Ni(OH)_2$ structure,[37] and stretching mode of Fe–O,[38] respectively. To further check the chemical state of the as-deposited Ni–Fe LDH, XPS was performed. The high-resolution XPS spectra of Fe 2p and Ni 2p are presented with fitting in Fig. 2e and f. For the Fe 2p spectrum, there are two major spin–orbital peaks at the binding energies of 723.5 eV and 710.5 eV, which are assigned to Fe^{3+} $2p_{1/2}$ and $2p_{3/2}$ orbitals, respectively.[39] Another peak located at 716.0 eV is associated with the satellite peak.[27] As for the Ni 2p spectrum, the two peaks at 873.2 eV and 855.4 eV are assigned to Ni^{2+} $2p_{1/2}$ and $2p_{3/2}$ orbitals, accompanied by two shake-up satellite peaks at 879.1 eV and 860.8 eV.[40] The broad band around 532 eV in the O 1s spectrum (Fig. S3†) corresponds to the lattice oxygen (O^{2-}), hydroxyl groups, and oxygen vacancies.[41,42] From the above systematic analyses on the morphology and chemical compositions by Auger, TEM, XRD, Raman and XPS, it is seen that the Ni–Fe LDH can be directly grown on a graphene/Si Schottky junction by electrodeposition and exhibits high-quality interfaces and excellent integration, which is important for high-performance PEC device applications.

Next, PEC ammonia conversion from nitrate solutions based on the Ni–Fe LDH/graphene/Si heterojunction devices was performed in a standard setup, where the working and counter electrodes were separated by a Nafion membrane. A Pt wire and Ag/AgCl electrode were used as the counter and reference electrodes, respectively. A sunlight simulator (AM 1.5G, 100 mW cm^{-2}) was used as a light source. 0.5 M Na_2SO_4 electrolytes with different concentrations of $NaNO_3$ ranging from 0.01 M to 0.5 M

were prepared. The schematic illustration for the PEC measurement is shown in Fig. 3a. The PEC polarization curves and corresponding faradaic efficiencies of the Ni–Fe LDH/graphene/Si junction measured in the electrolytes with different nitrate concentrations are shown in Fig. S4.† It is found that the highest faradaic efficiency occurs with 0.1 M nitrate concentration at potentials ranging from −0.15 V to −0.45 V. Therefore, we chose the electrolyte with 0.1 M nitrate concentration for further PEC analyses. Fig. 3b shows the representative polarization curves from linear sweep voltammetry (LSV) of the Ni–Fe LDH/graphene/Si junction photocathode at 0.1 M nitrate. For comparison, a dark cathode
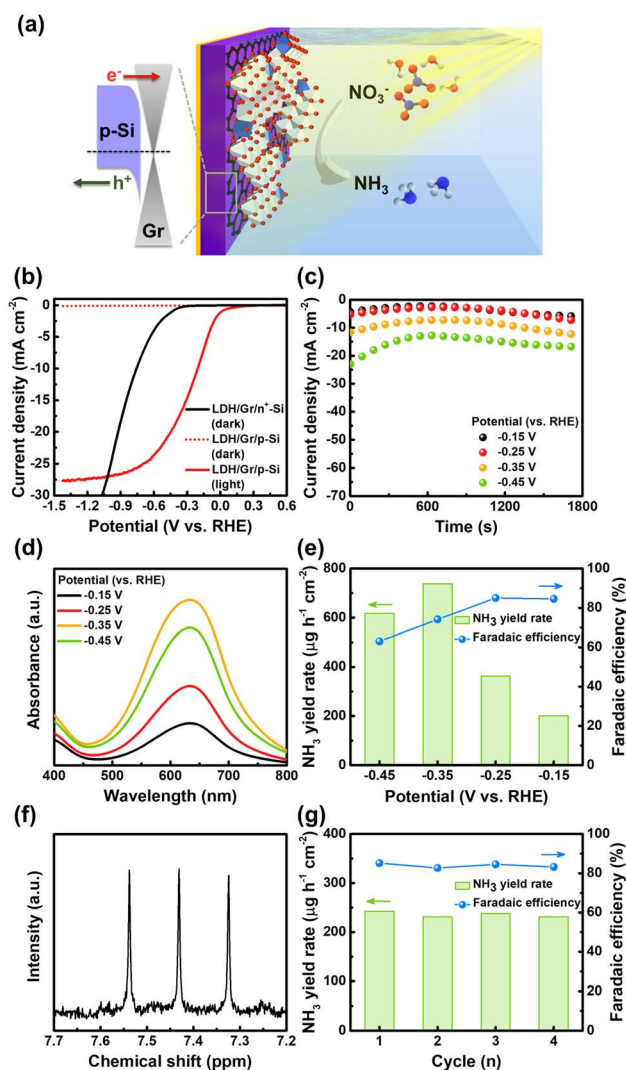

Fig. 3 PEC NTRR performances of the Ni–Fe LDH/graphene/Si heterojunction photocathode. (a) Schematic illustration for the PEC measurement of the Ni–Fe LDH/graphene/Si heterojunction photocathode. (b) Polarization curves in a 0.5 M Na_2SO_4 electrolyte with 0.1 M $NaNO_3$. (c) Chronoamperometric curves in −0.15 V, −0.25 V, −0.35 V, and −0.45 V (vs. RHE). (d) The corresponding absorbance spectra of sample electrolytes after chronoamperometric measurements by indophenol blue tests. (e) The calculated faradaic efficiency and NH_3 yield rate at various potentials. (f) The NMR ^1H spectrum of the electrolyte under −0.25 V. (g) The stability and reversibility test over four consecutive cycles at −0.15 V.

11182 | J. Mater. Chem. A, 2023, 11, 11179–11186

This journal is © The Royal Society of Chemistry 2023

consisting of the Ni–Fe LDH on the graphene/n$^+$-Si (heavily doped n-Si) junction is also shown, representing the corresponding EC NTRR performance of the Ni–Fe LDH catalyst. The Ni–Fe LDH/graphene/n$^+$-Si exhibits an onset potential of −0.44 V *vs.* RHE, where the onset potential is defined as the potential at a cathodic current density of −1 mA cm^{-2}. Under light illumination, the Ni–Fe LDH/graphene/p-Si junction photocathode exhibits an onset potential of 0.01 V *vs.* RHE and a positive shift of 550 mV at maximum compared to the dark cathode (Ni–Fe LDH/graphene/n$^+$-Si). The positive shift at the onset potential of the polarization curve mainly results from the sufficiently high photovoltage generation of the graphene/Si Schottky junction under light illumination.[43] Subsequently, chronoamperometric current density curves of the Ni–Fe LDH/graphene/Si junction for the NTRR were recorded over different potentials (−0.15, −0.25, −0.35 and −0.45 V) under light illumination, as shown in Fig. 3c. The production of ammonia during the tests was detected and quantified using the indophenol blue method. Fig. 3d shows the ultraviolet-visible (UV-Vis) spectra of the corresponding samples stained with indophenol blue test agents after recording time-dependent curves at different potentials. The intensities of the peaks (at a wavelength of 635 nm) are found to increase with increasing potential and reached the highest value at −0.35 V *vs.* RHE, signifying the increased ammonia formation with increasing potential. Further increasing the potential to −0.45 V results in reduced absorption peak intensity. Besides, at these operating potentials, the analyses of the additional by-product of NO$_2^-$ were also performed. It was found to be only 1% to 3% by using Griess test agents (Table S1†) but no hydrazine was detected by the Watt and Chrisp test in this system.[44] Fig. 3e shows the faradaic efficiency and NH$_3$ yield rate distribution over different potentials. The faradaic efficiency was found to be 84.57% at −0.15 V and the highest faradaic efficiency of 85.0% was reached at −0.25 V, where the corresponding yield rates of NH$_3$ are 200.48 μg h^{-1} cm^{-2} and 363.01 μg h^{-1} cm^{-2} at −0.15 V and −0.25 V, respectively. As the potential is further increased to −0.35 V and −0.45 V, the faradaic efficiencies decrease to 74.1% at −0.35 V and 63.0% at −0.45 V, although the corresponding NH$_3$ yield rates increase to 738.40 μg h^{-1} cm^{-2} and 617.51 μg h^{-1} cm^{-2}, respectively. This is mainly attributed to the enhanced competing HER process, which plays a more dominant role at the more negative potentials. To verify the formation of ammonia, the electrolyte solution obtained from the Ni–Fe LDH/graphene/Si junction photocathode operated at −0.25 V for two hours was further validated by nuclear magnetic resonance (NMR) spectroscopy. Fig. 3f shows the NMR spectrum of three peaks resolved in the range from the chemical shift of 7.3 to 7.6 ppm. The NMR signature confirms the formation of ammonia in the ^{1}H spectrum[11] during the PEC NTRR when Ni–Fe LDH/graphene/Si is employed as a working electrode under light illumination. Moreover, stability and reversibility are two other important factors for employing the Ni–Fe LDH/graphene/Si PEC device in practical nitrate-to-ammonia conversion. Fig. 3g shows the result of the stability and reversibility of the Ni–Fe LDH/graphene/Si junction photocathode, where the NTRR was scrutinized over four consecutive cycles at

−0.15 V. The operation time of each cycle is two hours. The faradaic efficiency and NH$_3$ yield rate are unaltered over four consecutive cycles, indicating the stability of the Ni–Fe LDH/graphene/Si junction photoelectrode towards efficient PEC nitrate-to-ammonia conversion.

To achieve an efficient PEC conversion, another essential prerequisite for the photoelectrodes is to enhance the light-harvesting efficiency. Although Si has a relatively low bandgap that enables the absorption of a wide solar spectrum, the large reflection of the conventional planar Si limits the light-harvesting efficiency. Hence, we utilized 3D pyramid Si to replace the planar Si to fabricate the Ni–Fe LDH/graphene/pyramid Si junction photocathode to further enhance the PEC NTRR conversion efficiency. To fabricate a 3D pyramid-like graphene/Si Schottky junction photoelectrode, we modified the transfer method that we developed in our previous work.[17] Through the facile electrodeposition method, the Ni–Fe LDH can also directly grow on the surface of the 3D textured graphene/Si Schottky junction as shown in Fig. 4a. The corresponding reflectance spectra of planar Si, graphene/planar Si, Ni–Fe LDH/graphene/planar Si, and Ni–Fe LDH/graphene/pyramid Si are shown in Fig. 4b. A UV-Vis spectrometer equipped with an integrating sphere was used to collect the scattering light from the Si surface to obtain these reflectance spectra. Both the planar Si and the graphene/planar Si junction devices show a similar reflectance spectrum with a slightly reduced reflectance at the graphene/Si photocathode compared to that of the pristine Si electrode. After the electrodeposition of the Ni–Fe LDH on the graphene/planar Si Schottky junction,
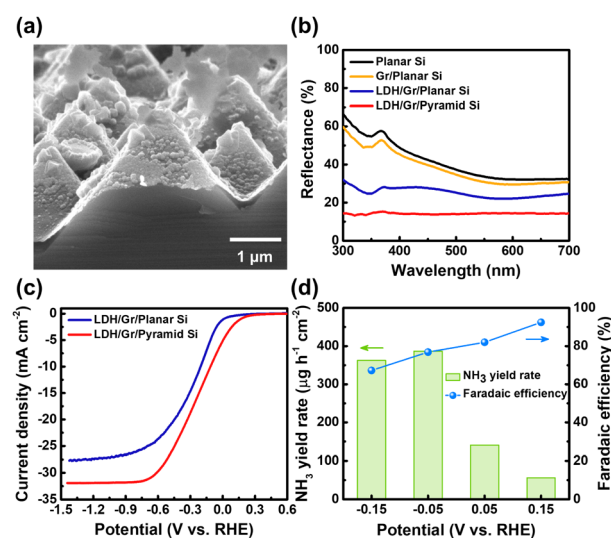

Fig. 4 Ni–Fe LDH/graphene/pyramid Si heterojunction photocathode. (a) The morphology image of Ni–Fe LDH deposited on the graphene/pyramid Si junction. (b) The reflectance spectra of the planar Si, graphene/planar Si, Ni–Fe LDH/graphene/planar Si, and Ni–Fe LDH/graphene/pyramid Si heterojunctions. (c) Polarization curves of Ni–Fe LDH/graphene/Si with planar and pyramid Si in a 0.5 M Na$_2$SO$_4$ electrolyte with 0.1 M NaNO$_3$. (d) The corresponding calculated faradaic efficiency and NH$_3$ yield rate of the Ni–Fe LDH/graphene/pyramid Si heterojunction device at −0.15 V, −0.05 V, 0.05 V, and 0.15 V (*vs.* RHE).

a significant reduction of the reflectance over a broad wavelength range is observed compared to that of the graphene/planar Si junction. The result suggests that the thin Ni–Fe LDH may also serve as an anti-reflective coating layer for the graphene/Si photocathodes due to the graded refractive index effect from the nanostructured Ni–Fe LDH layer.[27] In addition, because the Ni–Fe LDH is a semiconductor catalyst with a band gap of ~2 eV,[45] the reduced reflectance of the Ni–Fe LDH/graphene/planar Si device at shorter wavelengths may be attributed to enhanced light absorption above the band gap. For the Ni–Fe LDH/graphene/pyramid Si Schottky junction, the reflectance is further reduced by ~10% (at a wavelength of 450 nm) compared to the Ni–Fe LDH/graphene/planar Si counterpart, due to the enhanced light-trapping efficiency at the 3D pyramid-like Si structure. Fig. 4c shows the polarization curves of the photocathodes with Ni–Fe LDH directly grown on the planar and pyramid graphene/Si Schottky junction devices. The PEC NTRR was performed under the same conditions with 0.1 M $NaNO_3$ for both the planar and pyramid Si photocathodes under simulated AM 1.5G illumination. The Ni–Fe LDH/graphene/pyramid Si Schottky junction photocathode exhibits a positive shift by 158 mV with an onset potential of 0.17 V vs. RHE (at a cathodic current density of -1 mA cm^{-2}) and an increase of the saturated photocurrent density from -27.7 mA cm^{-2} to -31.9 mA cm^{-2}, due to the enhanced light-harvesting efficiency as compared to the Ni–Fe LDH/graphene/planar Si Schottky junction counterpart. Fig. 4d shows the corresponding faradaic efficiencies and NH_3 yield rates of the Ni–Fe LDH/graphene/pyramid Si junction photocathode measured at the potentials of -0.15, -0.05, 0.05 and 0.15 V vs. RHE. The corresponding chronoamperometric current density curves and UV-Vis spectra with the indophenol indicator are provided in Fig. S5.† The Ni–Fe LDH/graphene/pyramid Si Schottky junction device exhibits outstanding PEC NTRR performance with the highest faradaic efficiency of 92.5% that can be achieved at a potential of 0.15 V vs. RHE. It has been reported that the unburied transition metal atoms of LDH are highly active and mainly responsible for the catalytic activities when oxygen vacancies exist.[42,46] Here, we performed the density functional theory (DFT) calculation of adsorption configurations and their corresponding Gibbs free energies on the basal plane of Ni–Fe LDH models consisting of oxygen vacancies. The calculation details and result are presented in the ESI.† The DFT calculation result shows that the reaction barrier of the rate-determining step results from NO* to N* intermediates. It is found that the oxygen vacancy in the Ni–Fe LDH catalyst may effectively lower the reaction barrier for the NTRR, in contrast to a perfect basal plane lacking catalytic ability. Combined with the sufficiently high photovoltage generation of the graphene/Si Schottky junction under light illumination, the Ni–Fe LDH/graphene/Si heterojunction exhibits efficient PEC nitrate-to-ammonia conversion.

Conclusions

In summary, we have demonstrated a Ni–Fe LDH/graphene/Si Schottky junction photocathode for efficient PEC nitrate to

ammonia conversion. The direct growth of the Ni–Fe LDH catalyst on the surface of the graphene/Si Schottky junction enables efficient photogenerated carrier transport and transfer between the photocathode and catalyst. Both the planar and 3D pyramid Ni–Fe LDH/graphene/Si Schottky junction devices exhibit excellent PEC NTRR conversion efficiencies and stability. The facile integration of catalysts and graphene/Si Schottky junction photoelectrodes, bridged by a single atomic layer of graphene, provides an effective strategy to achieve an efficient and stable solar-to-ammonia conversion and can be applied to other solar-to-fuel conversions such as water splitting or CO_2 reduction.

Experimental section

Material characterization

Raman spectroscopy was performed with an Andor Kymera 193i-B2 spectrometer and an Andor iDus416 detector. The excitation source was a 532 nm Nd:YAG continuous-wave laser and an Olympus 50× objective lens was used. The SEM image was collected on a NOVA NANO SEM 450 (15 kV, spot size 3.0). Auger electron spectroscopy and mapping were conducted on a JEOL JAMP 9510F. The TEM image and SAED pattern were collected on a JEOL 2010F. The TEM specimen was cut with a FIB (FEI Helios 600i). XRD was performed by using a Bruker D8 Advance X-ray diffractometer (Cu Kα1) with a step size of 0.01°, a scan rate of 0.5 s per step, and an operating voltage of 40 kV. The XPS analysis was performed on a Thermo Scientific Theta Probe (aluminum anode). The reflectance spectra were acquired by using a Hitachi U-4100 with an integrating sphere.

Fabrication of the graphene/Si heterojunction

The PEC devices were fabricated on a p-type lightly doped Si substrate (1–10 ohm cm). The backside electrode was deposited with a thermal evaporator with 5 nm Cr and 60 nm Au immediately after buffer oxide etching (BOE, 6 : 1 volume ratio of 40% NH_4F and 49% HF) removed the native oxide on the backside of the Si substrate surface. The single-layer graphene was grown on copper foil by using a low-pressure CVD system. For the planar Si device, the single-layer graphene was transferred by the PMMA-assisted transfer method (950 PMMA A6, MicroChem) onto the front side of the Si substrate. The PMMA was coated on the as-grown graphene and floated onto $FeCl_3$ (99.99%, Sigma-Aldrich) aqueous solution to etch the copper foil. Then, PMMA/graphene was rinsed with water at least three times and transferred on the Si target substrate. The PMMA was typically removed in acetone overnight. For the pyramid Si device, the graphene was transferred by the EVA-assisted method. The EVA solution was prepared by dissolving vinyl acetate (Sigma-Aldrich) into o-xylene (99%, Sigma-Aldrich). The removal of EVA was conducted in a hot o-xylene bath at 50 °C for 15 min.

Electrodeposition of Ni–Fe LDH on the graphene/Si heterojunction

The Ni–Fe LDH was electrodeposited on the graphene/Si junction. A standard three-electrode EC system (Metrohm Autolab

11184 | J. Mater. Chem. A, 2023, **11**, 11179–11186

This journal is © The Royal Society of Chemistry 2023

PGSTAT302N) was used with a customized Teflon cell. Graphene/Si acted as the working electrode. Copper tape and conductive silver adhesive were used to wire the device to the potentiostat. A Pt wire and Ag/AgCl (3 M KCl) electrode (Metrohm) were used as counter and reference electrodes, respectively. The electrodeposition solution was prepared from nickel sulfate hexahydrate (98%, Acros), iron sulfate heptahydrate (99%, Acros), boric acid (99.5%, Acros), and sodium chloride (99%, Alfa Aesar) in deionized water. The electrodeposition time was 10 seconds under -8 V (*vs.* Ag/AgCl), which is applied on the graphene/Si working electrode. A rinsing process in water was followed for surface cleaning.

Photoelectrochemical measurement

The PEC measurements were performed in a three-electrode cell by using a Metrohm Autolab PGSTAT302N with an EIS module. An Ag/AgCl (3 M KCl) electrode and Pt wire were used as the reference and counter electrodes, respectively. The electrolyte was prepared with Na_2SO_4 (99.0%, Merck) and $NaNO_3$ (99.0%, Merck) in deionized water. The EC cell system was under light illumination (AM 1.5 G, Newport Co.). To restrict the reaction area, the device was blanketed by chemical-resistant tape with a reaction window area of 16 mm^2 at the center of the Si chip. The polarization curves were recorded with a scan rate of 5 mV s^{-1} in LSV measurement. The EIS analysis was performed by setting the ac signals with an amplitude of 5 mV and the frequency ranging from 10^6 to 10^{-2} Hz. The amount of ammonia was determined by the indophenol blue method. The test agent for the indophenol blue method was prepared with 100 μL of NaOCl containing 1 M NaOH (98%, Fisher), 100 μL of 0.5 M phenol, and 50 μL of 0.002 M $Na_2[Fe(CN)_3N_2]$. The 1 mL sample electrolyte was added to the test agent and mixed gently for reaction. After 30 min reaction in the dark, absorbance spectroscopy measurement was performed using a LAMBDA 365 UV-Vis spectrophotometer (PerkinElmer). The values of absorbance at 635 nm in the spectra were recorded for establishing the standard concentration–absorbance calibration curve and calculating the faradaic efficiency and yield of NH_3. To detect the NO_2^-, Griess reagent (Thermo Fisher) was used. The values of absorbance at 540 nm were for the calibration curve and also the faradaic efficiency and yield determination. For hydrazine detection, the Watt and Chrisp method and the hydrazine test agent (Merck) were adopted. The values of absorbance at 450 nm were recorded.

Author contributions

Chun-Hao Chiang: validation, investigation, writing – original draft, and visualization. Yu-Ting Kao: validation, investigation, and visualization. Po-Hsien Wu: validation and investigation. Ting-Ran Liu: validation and investigation. Jia-Wei Lin: formal analysis. Po-Tuan Chen: formal analysis and resources. Jr-Wen Lin: validation and Investigation. Shan-Chiao Yang: investigation. Hsuen-Li Chen: investigation and resources. Shivaraj B. Patil: investigation. Di-Yan Wang: conceptualization, resources, and writing – review & editing. Chun-Wei Chen: conceptualization, resources, writing – review & editing, and supervision.

Conflicts of interest

There are no conflicts of interest to declare.

Acknowledgements

References

1 X. Zhao, G. Hu, G.-F. Chen, H. Zhang, S. Zhang and H. Wang, *Adv. Mater.*, 2021, **33**, 2007650.

2 D. Chanda, R. Xing, T. Xu, Q. Liu, Y. Luo, S. Liu, R. A. Tufa, T. H. Dolla, T. Montini and X. Sun, *Chem. Commun.*, 2021, **57**, 7335–7349.

3 B. Yang, W. Ding, H. Zhang and S. Zhang, *Energy Environ. Sci.*, 2021, **14**, 672–687.

4 J. Wang, T. Feng, J. Chen, V. Ramalingam, Z. Li, D. M. Kabtamu, J.-H. He and X. Fang, *Nano Energy*, 2021, **86**, 106088.

5 C. Lv, L. Zhong, H. Liu, Z. Fang, C. Yan, M. Chen, Y. Kong, C. Lee, D. Liu, S. Li, J. Liu, L. Song, G. Chen, Q. Yan and G. Yu, *Nat. Sustain.*, 2021, **4**, 868–876.

6 X. Fu, X. Zhao, X. Hu, K. He, Y. Yu, T. Li, Q. Tu, X. Qian, Q. Yue, M. R. Wasielewski and Y. Kang, *Appl. Mater. Today*, 2020, **19**, 100620.

7 Y. Wang, C. Wang, M. Li, Y. Yu and B. Zhang, *Chem. Soc. Rev.*, 2021, **50**, 6720–6733.

8 G.-F. Chen, Y. Yuan, H. Jiang, S.-Y. Ren, L.-X. Ding, L. Ma, T. Wu, J. Lu and H. Wang, *Nat. Energy*, 2020, **5**, 605–613.

9 R. Jia, Y. Wang, C. Wang, Y. Ling, Y. Yu and B. Zhang, *ACS Catal.*, 2020, **10**, 3533–3540.

10 Y. Wang, A. Xu, Z. Wang, L. Huang, J. Li, F. Li, J. Wicks, M. Luo, D.-H. Nam, C.-S. Tan, Y. Ding, J. Wu, Y. Lum, C.-T. Dinh, D. Sinton, G. Zheng and E. H. Sargent, *J. Am. Chem. Soc.*, 2020, **142**, 5702–5708.

11 Y. Wang, W. Zhou, R. Jia, Y. Yu and B. Zhang, *Angew. Chem., Int. Ed.*, 2020, **59**, 5350–5354.

12 F. Du, J. Li, C. Wang, J. Yao, Z. Tan, Z. Yao, C. Li and C. Guo, *Chem. Eng. J.*, 2022, **434**, 134641.

13 M. A. Marwat, M. Humayun, M. W. Afridi, H. Zhang, M. R. Abdul Karim, M. Ashtar, M. Usman, S. Waqar, H. Ullah, C. Wang and W. Luo, *ACS Appl. Energy Mater.*, 2021, **4**, 12007–12031.

14 M. Kan, Q. Wang, S. Hao, A. Guan, Y. Chen, Q. Zhang, Q. Han and G. Zheng, *J. Phys. Chem. C*, 2022, **126**, 1689–1700.

This journal is © The Royal Society of Chemistry 2023

J. Mater. Chem. A, 2023, **11**, 11179–11186 | **11185**

15 H. E. Kim, J. Kim, E. C. Ra, H. Zhang, Y. J. Jang and J. S. Lee, *Angew. Chem., Int. Ed.*, 2022, **61**, e202204117.

16 S. Zhou, K. Sun, C. Y. Toe, J. Yin, J. Huang, Y. Zeng, D. Zhang, W. Chen, O. F. Mohammed, X. Hao and R. Amal, *Adv. Mater.*, 2022, **34**, 2201670.

17 C.-K. Ku, P.-H. Wu, C.-C. Chung, C.-C. Chen, K.-J. Tsai, H.-M. Chen, Y.-C. Chang, C.-H. Chuang, C.-Y. Wei, C.-Y. Wen, T.-Y. Lin, H.-L. Chen, Y.-S. Wang, Z.-Y. Lee, J.-R. Chang, C.-W. Luo, D.-Y. Wang, B. J. Hwang and C.-W. Chen, *Adv. Energy Mater.*, 2019, **9**, 1901022.

18 W. J. Dong, I. A. Navid, Y. Xiao, J. W. Lim, J.-L. Lee and Z. Mi, *J. Am. Chem. Soc.*, 2021, **143**, 10099–10107.

19 K. Peramaiah, V. Ramalingam, H.-C. Fu, M. M. Alsabban, R. Ahmad, L. Cavallo, V. Tung, K.-W. Huang and J.-H. He, *Adv. Mater.*, 2021, **33**, 2100812.

20 R. Fan, W. Dong, L. Fang, F. Zheng and M. Shen, *J. Mater. Chem. A*, 2017, **5**, 18744–18751.

21 I. A. Digdaya, G. W. P. Adhyaksa, B. J. Trzesniewski, E. C. Garnett and W. A. Smith, *Nat. Commun.*, 2017, **8**, 15968.

22 J. Yang, K. Walczak, E. Anzenberg, F. M. Toma, G. Yuan, J. Beeman, A. Schwartzberg, Y. Lin, M. Hettick, A. Javey, J. W. Ager, J. Yano, H. Frei and I. D. Sharp, *J. Am. Chem. Soc.*, 2014, **136**, 6191–6194.

23 H. Yi, S. Liu, C. Lai, G. Zeng, M. Li, X. Liu, B. Li, X. Huo, L. Qin, L. Li, M. Zhang, Y. Fu, Z. An and L. Chen, *Adv. Energy Mater.*, 2021, **11**, 2002863.

24 Y. Wang, D. Yan, S. E. Hankari, Y. Zou and S. Wang, *Adv. Sci.*, 2018, **5**, 1800064.

25 W. Li, P. Hou, Z. Wang and P. Kang, *Sustain. Energy Fuels*, 2019, **3**, 1455–1460.

26 B. Guo, A. Batool, G. Xie, R. Boddula, L. Tian, S. U. Jan and J. R. Gong, *Nano Lett.*, 2018, **18**, 1516–1521.

27 J. Zhao, L. Cai, H. Li, X. Shi and X. Zheng, *ACS Energy Lett.*, 2017, **2**, 1939–1946.

28 D.-Y. Wang, I.-S. Huang, P.-H. Ho, S.-S. Li, Y.-C. Yeh, D.-W. Wang, W.-L. Chen, Y.-Y. Lee, Y.-M. Chang, C.-C. Chen, C.-T. Liang and C.-W. Chen, *Adv. Mater.*, 2013, **25**, 4521–4526.

29 X. Kong, L. Zhang, B. Liu, H. Gao, Y. Zhang, H. Yan and X. Song, *RSC Adv.*, 2019, **9**, 863–877.

30 R. R. Nair, P. Blake, A. N. Grigorenko, K. S. Novoselov, T. J. Booth, T. Stauber, N. M. Peres and A. K. Geim, *Science*, 2008, **320**, 1308.

31 P.-H. Ho, W.-C. Lee, Y.-T. Liou, Y.-P. Chiu, Y.-S. Shih, C.-C. Chen, P.-Y. Su, M.-K. Li, H.-L. Chen, C.-T. Liang and C.-W. Chen, *Energy Environ. Sci.*, 2015, **8**, 2085–2092.

32 P.-H. Ho, Y.-T. Liou, C.-H. Chuang, S.-W. Lin, C.-Y. Tseng, D.-Y. Wang, C.-C. Chen, W.-Y. Hung, C.-Y. Wen and C.-W. Chen, *Adv. Mater.*, 2015, **27**, 1724–1729.

33 H. Yang, S. Luo, Y. Bao, Y. Luo, J. Jin and J. Ma, *Inorg. Chem. Front.*, 2017, **4**, 1173–1181.

34 X. Yu, M. Zhang, W. Yuan and G. Shi, *J. Mater. Chem. A*, 2015, **3**, 6921–6928.

35 X. Li, J. Zai, Y. Liu, X. He, S. Xiang, Z. Ma and X. Qian, *J. Power Sources*, 2016, **325**, 675–681.

36 C. Johnston and P. R. Graves, *Appl. Spectrosc.*, 1990, **44**, 105–115.

37 M. W. Louie and A. T. Bell, *J. Am. Chem. Soc.*, 2013, **135**, 12329–12337.

38 T. Nguyen and M. F. Montemor, *J. Mater. Chem. A*, 2018, **6**, 2612–2624.

39 X. Zhao, Y. Wang, Y. Zhang, S. Luo, H. Zhang and D. Y. C. Leung, *ChemSusChem*, 2022, **15**, e202102614.

40 B. Eftekharinia, H. Pezeshki and A. Dabirian, *ACS Appl. Mater. Interfaces*, 2020, **12**, 17424–17435.

41 Z. Xu, Y. Ying, G. Zhang, K. Li, Y. Liu, N. Fu, X. Guo, F. Yu and H. Huang, *J. Mater. Chem. A*, 2020, **8**, 26130–26138.

42 Y. Tang, Q. Liu, L. Dong, H. B. Wu and X.-Y. Yu, *Appl. Catal., B*, 2020, **266**, 118627.

43 W. Yang, R. R. Prabhakar, J. Tan, S. D. Tilley and J. Moon, *Chem. Soc. Rev.*, 2019, **48**, 4979–5015.

44 G. W. Watt and J. D. Chrisp, *Anal. Chem.*, 1952, **24**, 2006–2008.

45 J. Yan, X. Zhang, W. Zheng and L. Y. S. Lee, *ACS Appl. Mater. Interfaces*, 2021, **13**, 24723–24733.

46 Y. Zhou, W. Zhang, J. Hu, D. Li, X. Yin and Q. Gao, *ACS Sustain. Chem. Eng.*, 2021, **9**, 7390–7399.